Supplementary Information: Nanoscale heterogeneity promotes energy dissipation in bone

KUANGSHIN TAI,[1*] MING DAO,[1*] SUBRA SURESH,[1,2] AHMET PALAZOGLU,[3] & AND CHRISTINE ORTIZ[1]

[1]Department of Materials Science and Engineering, [2]Division of Biological Engineering, Massachusetts Institute of Technology, 77 Massachusetts Avenue, Cambridge, Massachusetts 02139, USA
[3]Department of Chemical Engineering and Materials Science, University of California, One Shields Avenue, Davis, CA 95616, USA
Both authors contributed equally to this work.

1. Effect of Surface Roughness and Topography

The possible role of surface roughness in influencing the nanoscale energy dissipation in bone was investigated both experimentally and computationally. The peak-to-valley heights of the topographical features measured from the tapping mode atomic force microscopy (AFM) images shown in Figs. 2a,d of the main manuscript (presumably mineral particles) were measured to be ~ 11.5 ± 9.1 nm and the average root mean square (rms) roughness was calculated to be ~ 11.5 nm over 2 μm × 2 μm scan areas. Hence, the average indentation depth was ~ 3× greater than the average topographical feature peak-to-valley height and rms surface roughness. Approximately 3000 AFM-based nanoindentation experiments (tetrahedral probe tip end radius, R_{tip} ~ 15 nm, equivalent cone angle 23.5º, measured by scanning electron microscopy and shown in Fig. 1 of the main manuscript) were carried out over a large range of the ratio, h_{max}/rms surface roughness (~2-16). Here, h_{max} was the depth at maximum load for a particular indent and the rms surface roughness was measured directly at each nanoindentation position (before nanoindentation) directly by tapping mode AFM imaging over a 100 nm × 100 nm square region. This point-by-point nanoscale rms surface roughness measurement taken at the exact position of nanoindentation and over the approximate size of the indent area is more accurate than employing a mean rms surface roughness value for the entire surface. Elastic modulus data (calculated using the commonly used Oliver-Pharr model[1] at each position) were separated into equal bins of 1 h_{max}/rms surface roughness and the data that fell within in each bin was used to calculate a coefficient of variation (COV = ratio of standard deviation to the mean). Fig. 1 is a plot of COV versus h_{max}/rms surface roughness for the AFM-based nanoindentation data (black square symbols). These data show that the COV stays within 0.3-0.4 for the entire range of h_{max}/rms surface roughness and is in fact statistically independent of h_{max}/rms surface roughness. An ANOVA variance test was performed using the O'Brien method[2] to test for homogeneity of variances between the different COV groups relative to one another. Using this analysis, it was shown that the assumption for homoscedasticity was met ($F = 1.0113$, $p > 0.05$), i.e. that there was no overall statistically significant trend for the dependence of the COV on h_{max}/rms surface roughness. Fig. 1 also compares AFM-based experimental nanoindentation data with experiments carried out on similar samples with an instrumented nanoindentor (*Hysitron, Inc.*) and Berkovich probe tip (square pyramidal, R_{tip} ~ 180 nm, included angle 142.3º).[3] In this case, the R_{tip} was iteratively determined through a series of FEA simulations compared to experimental indentations on fused silica. These data show an increase in the COV for h_{max}/rms surface roughness < 5. It is unclear whether this effect is a surface roughness effect or is convoluted by a length-scale dependent homogenization effect due to the hierarchical nanostructure of bone (i.e. the response of local, nanoscale mechanically differing regions which are averaged into a more continuum-like response at larger contact areas). To determine the origin of the increased COV at smaller h_{max}/rms surface roughness values for the instrumented indentation data, further theoretical work is needed which would take into account the nanoscale structure of the material, the probe tip geometry and size, and the maximum load and depth (such research is ongoing and beyond the scope of this manuscript). As described in the main manuscript, the increased COV of the AFM-based experiments compared to the larger length scale instrumented indentation data is attributed to the exceedingly sharp probe tip which is able to feel local nanoscale heterogeneities for example, nanoscale interfaces and the effect of individual nanoscale constituents. A two-dimensional indentation modulus map for h_{max}/rms surface roughness >10 is shown in Fig. 2 which shows a COV of 0.34, which is consistent with Fig. 1.

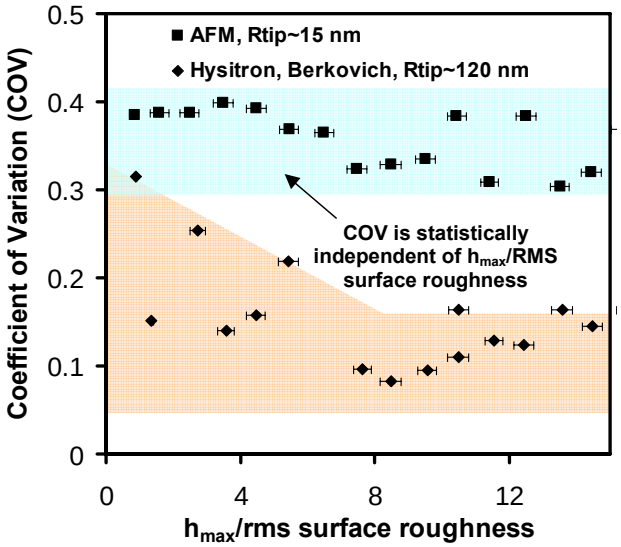

Figure 1. COV versus h_{max}/rms surface roughness for AFM-based nanoindentation experiments on bovine cortical bone with loading axis perpendicular to the long bone axis (tetrahedral probe tip, R_{tip}~ 15 nm, total number of experiments, *n* = 3215, square symbols). These data are compared to instrumented nanoindentation experiments (diamond symbols) performed by us (Berkovich probe tip, R_{tip} ~ 180 nm, *n*=750).

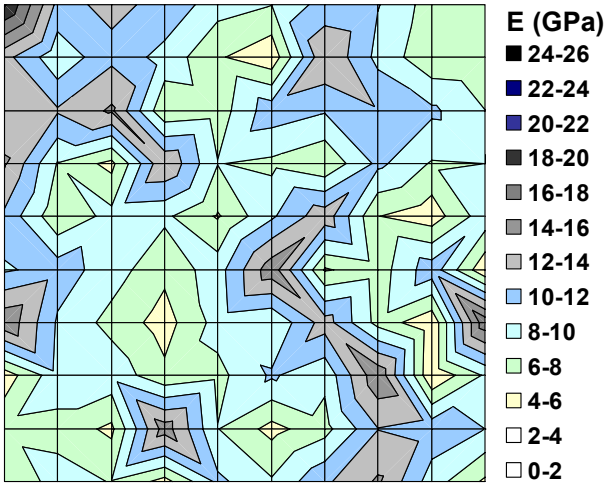

Figure 2. Two-dimensional contour map of indentation modulus for bovine cortical bone with the loading axis perpendicular to the long bone axis using a tetrahedral AFM probe tip (R_{tip}~15 nm) for h_{max}/rms surface roughness of 10.4 which yields a COV = 0.34. The distance between neighbouring indents (grid spacing) was chosen to be ~ 200 nm, sufficiently greater to avoid overlap of inelastic/residual stress zones.

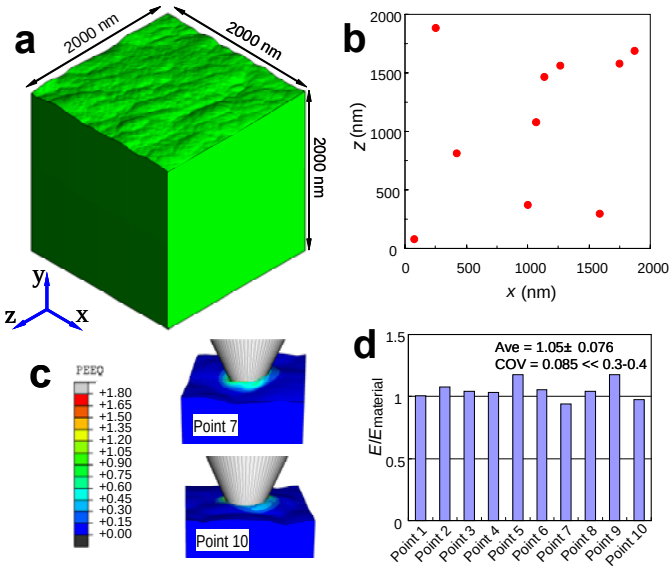

Figure 3. Full 3D FEA simulation results designed to assess the possible influence of surface roughness on deformation. a) The experimentally measured AFM height data was digitized and implemented in the 3D FEA model. b) 10 indentation points were chosen from a), where full 3D FEA simulations were performed at each selected point. c) Equivalent plastic strain contour plots at the maximum indentation depth ($3h_{RMS}$ = 34.5 nm) for Point 7 and 10, respectively. d) Indentation modulus extracted using the load-depth curves obtained by FEA simulations. In all the simulations, the input modulus and yield stress (8.55 GPa and 395 MPa, respectively) were chosen as the average for the data taken from the map in Fig. 2b of the main manuscript, where the loading axis was perpendicular to the long bone axis. Here, the AFM probe tip was approximated as a cone tip with an included half angle of 23.5º and a 15nm tip radius.

A 3D elasto-plastic finite element analysis (FEA) model was constructed directly from the experimental AFM height data which was digitized and inserted in the FEA software ABAQUS (Fig. 3). Assuming a homogeneous property distribution, we are able to separately quantify the effect of surface roughness on the nanomechanical experiments, based on the known experimentally measured surface roughness map. The maximum indentation depth was taken to be $3h_{rms}$. The COV calculated from virtually indenting with the AFM probe tip (approximated by a cone with a 23.5º half included angle and a 15 nm tip radius) at 10 randomly chosen locations on the (rough) surface was 0.085, which is markedly less than the experimentally measured COV (0.3-0.4). It should be noted that the Oliver-Pharr method[1] used to extract modulus values is primarily based on the unloading portion of the curve. Here, our results indicate that the experimentally measured large modulus variations can not be explained by surface roughness. Additionally, using either a pressure-sensitive or an anisotropic elasticity constitutive response does not change these conclusions (see below). As can be seen from the geometry and length scales of the deformed FEA meshes (Fig. 3c), for such a sharp probe tip, the D = 0 position measured experimentally is accurate and instead any surface roughness error in the present study would be due to the local topographical slope changing the contact area. However, as discussed above, this effect is very much smaller than the measured variations.

2. Effect of Anisotropy

Further finite element analyses were performed incorporating anisotropy and were found not to change the main result of the paper; i.e. that heterogeneity contributes to enhanced energy dissipation through increased ductility. The model incorporated transverse orthotropy using anisotropy ratios (AR ~1.5) estimated from ultrasonic velocity tests.[4] For the case where indentations were taken perpendicular to the long bone axis, elastic property values for the homogeneous case were: $E_1 = E_2 = 8.55$ GPa, $E_3 = 12.8$ GPa, $\nu_{12} = 0.42$, $\nu_{23} = \nu_{13} = 0.23$, $G_{12} = E_3/5$, $G_{13} = G_{23} = E_3/4$. For the heterogeneous case, Poisson's ratio values were taken to be the same as those in Rho et al., 1996,[4] but the inputs for E_3, G_{12}, G_{13}, and G_{23} were taken with reference to each of the modulus values prescribed from the experimental data. The inelastic equivalent strain comparing the homogeneous and heterogeneous cases for isotropic and anisotropic material models are visualized in Fig. 4. Plots of the inelastically strained area as a function of force as well as normalized energy dissipation comparing the different instances are shown in Fig. 5. In general, the difference in inelastically strained area between the homogeneous and heterogeneous maps for isotropic and anisotropic cases is similar, at 68% and 70%, respectively (Fig. 5a). The normalized energy dissipation variation between homogeneous and heterogeneous cases is also similar (Fig. 5b). Even though it does not change the main result of the manuscript, one noticeable distinction in incorporating anisotropy is that there is much larger overall inelasticity for anisotropic case. In light of this observation, our preliminary analyses suggest that anisotropic heterogeneity in bone is an area of research that requires future detailed studies.

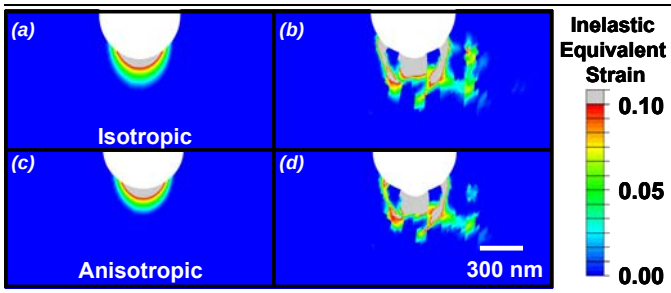

Figure 4. Visualization of the inelastic equivalent strain in the 4-point bend FEA simulations comparing a) isotropic homogeneous, b) isotropic heterogeneous, c) anisotropic homogeneous, and d) anisotropic heterogeneous models. The total displacement from the bottom portion of the entire mesh (Fig. 4a of main manuscript) was 1.95 µm. The heterogeneous map was taken from Fig. 2b of the main manuscript where the loading axis was perpendicular to the long bone axis.

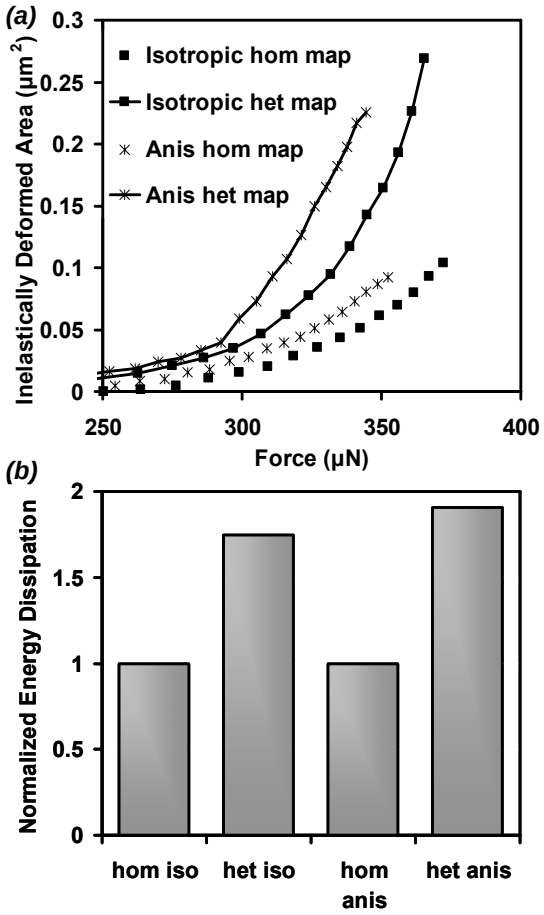

Figure 5. Plots of the *(a)* inelastically strained area as a function of force along with *(b)* energy dissipation that compares the isotropic and anisotropic material models for homogeneous and heterogeneous cases (taken from Fig. 2b of the main manuscript where the loading axis was perpendicular to the long bone axis) are shown here. The total displacement from the bottom portion of the entire mesh (Fig. 4a of main manuscript) was 1.95 µm.

3. Effect of Pressure Sensitivity

Pressure sensitivity was incorporated using the Mohr-Coulomb yield criterion where the friction angle was taken to be 15° (cohesion was calculated from the Mohr-Coulomb relationship based on the friction angle from our recently published study[5]) and assuming the constant yield strain criterion in the microstructure. The inelastic equivalent strain comparing the homogeneous and heterogeneous cases for the pressure-independent and pressure-sensitive material models are visualized in Fig. 6. Plots of the inelastically strained area as a function of force as well as the normalized energy dissipation comparing the different instances are shown in Fig. 7. Similar to when incorporating material anisotropy, the differences in inelastically strained area between the homogeneous and heterogeneous maps for each material model as well as the normalized energy dissipation variation are similar. Although the overall qualitative difference between homogeneous and heterogeneous cases is not affected, there appears to be a slight "bump" variation shown in Fig. 7a for the pressure sensitive model, due to lack of additional elements being yielded at the load force level of 325-340 µN for this microstructure under the Mohr-Coulomb yield criterion. Pressure-sensitive heterogeneity in bone is another valuable area of study worth more detailed examination for future research.

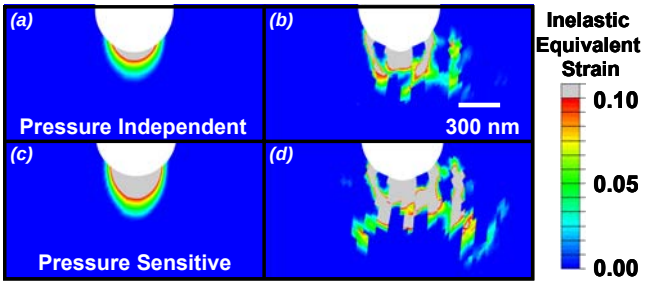

Figure 6. Predictions from 4-point bend FEA simulations comparing inelastic strain for; (a) pressure-independent homogeneous, (b) pressure-independent heterogeneous, (c) pressure-sensitive homogeneous, and (d) pressure-sensitive heterogeneous models. The displacement from the bottom of the mesh (Fig. 4a of main manuscript) was 1.95 µm. The heterogeneous map was taken from Fig. 2b of the main manuscript where the loading axis was perpendicular to the long bone axis.

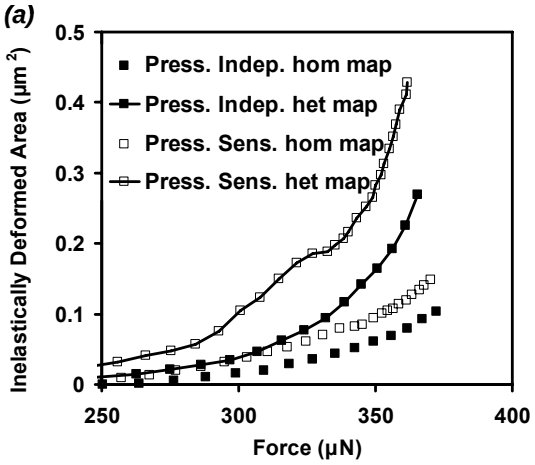

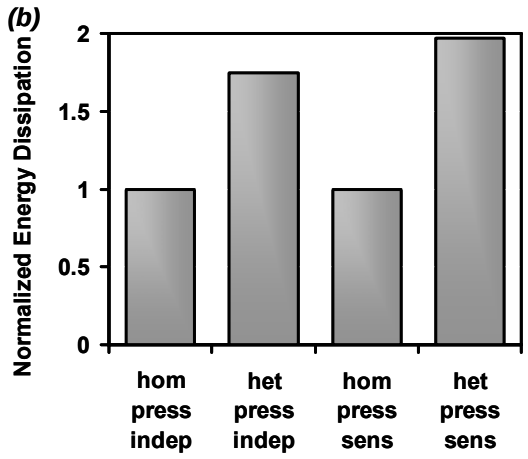

Figure 7. Plots of the *(a)* inelastically strained area as a function of force along with *(b)* energy dissipation that compares the pressure-independent to the pressure sensitive models for homogeneous and heterogeneous cases (taken from Fig. 2b of the main manuscript where the loading axis was perpendicular to the long bone axis). The displacement from the bottom of the mesh (Fig. 4a) was 1.95 μm.

4. Effect of Notch Diameter

The effect of notch diameter was incorporated assuming the same constant yield strain criterion as previously employed. The inelastic equivalent strain comparing the homogeneous and heterogeneous cases for different notch diameters of 300, 600, and 1200 nm are visualized in Fig. 8. Plots of the inelastically strained area as a function of force as well as the normalized energy dissipation comparing the different instances are shown in Fig. 9. Similar to the previous cases, the differences in inelastically strained area between the homogeneous and heterogeneous maps for each material model as well as the normalized energy dissipation variation are similar. Although the overall qualitative difference between homogeneous and heterogeneous cases is generally not affected, there appears to be an increase in the relative energy dissipation for the 300 nm notch size case in the ratio between heterogeneous to homogeneous models compared to that of the 600 and 1200 nm notch size models. This observation suggests a size or morphology effect contribution to energy dissipation and could merit further study.

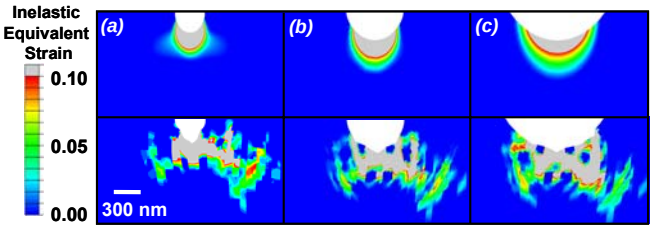

Figure 8. Equivalent inelastic strain for the 4-pont bend FEA virtual simulations which incorporated the heterogeneous nanoindentation data taken with the loading axis perpendicular to the long bone axis (Fig. 2b of main manuscript) where the 2 μm × 2 μm mechanical property map is placed in close proximity to a (a) 300 nm notch, (b) a 600 nm notch (as presented thus far), and (c) a 1200 nm notch in the plane of the long bone axis (the plane of the paper). The displacement from the bottom of the mesh (Fig. 4a of main manuscript) was 1.95 μm.

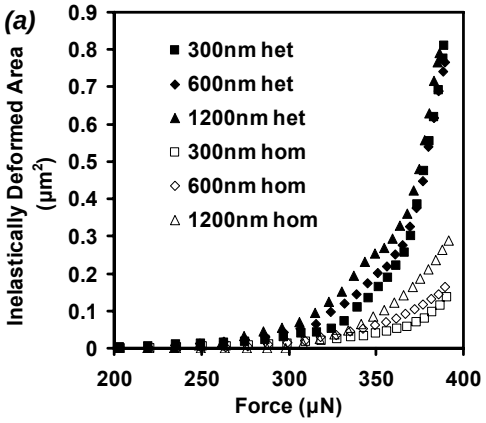

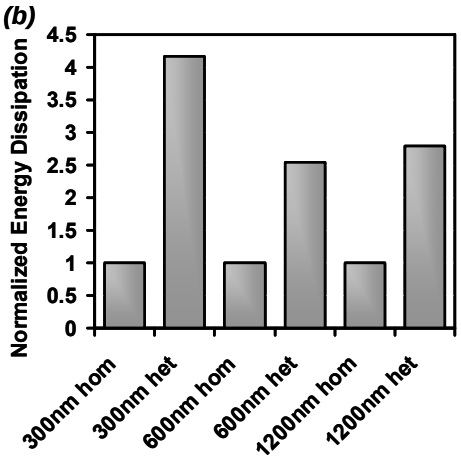

Figure 9. Plots of the *(a)* inelastically strained area as a function of force along with *(b)* energy dissipation that compares the 300, 600, and 1200 nm radius notch size models for homogeneous and heterogeneous cases (taken from Fig. 2b of the main manuscript where the loading axis was perpendicular to the long bone axis). The displacement from the bottom of the mesh (Fig. 4a of main manuscript) was 1.95 μm.

5. Shifted Notch Effects

The effect of shifting the location of the notch was incorporated assuming the same constant yield strain criterion as previously described. The inelastic equivalent strain comparing the homogeneous and heterogeneous cases for notches shifted up and down by 300 nm are visualized in Fig. 10. Plots of the inelastically strained area as a function of force as well as the normalized energy dissipation comparing the different instances are shown in Fig. 11. Similar to the previous cases, the relative differences in inelastically strained area between the homogeneous and heterogeneous maps for each material model, as well as in the normalized energy dissipation, are similar.

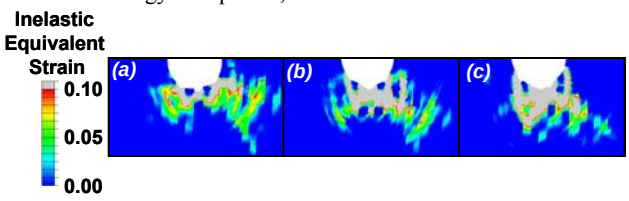

Figure 10. Equivalent inelastic strain for the 4-pont bend FEA virtual simulations which incorporated the heterogeneous

nanoindentation data taken with the loading axis perpendicular to the long bone axis (Fig. 2b of main manuscript) where the 2 μm x 2 μm mechanical property map is placed (a) shifted 300 nm down, (b) zero shift, (c) shifted up 300 nm in the plane of the long bone axis (the plane of the paper). The displacement from the bottom of the mesh (Fig. 4a of main manuscript) was 1.95 μm.

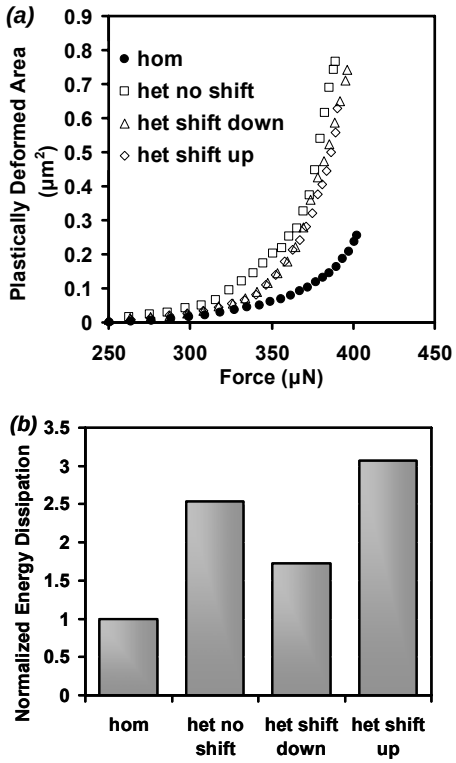

Figure 11. Plots of the *(a)* inelastically strained area as a function of force along with *(b)* energy dissipation that compares the models with the notch shifted up and down for homogeneous and heterogeneous cases. The heterogeneously mapped region employed nanoindentation data taken with the loading axis perpendicular to the long bone axis (Fig. 2b of main manuscript). The displacement from the bottom of the mesh (Fig. 4a of main manuscript) was 1.95 μm.

6. Effect of Tip Angle (11°)

The cantilever and AFM probe tip are angled with an 11° tilt with respect to the sample surface. To estimate the influence of this tilting towards the modulus extraction, we have performed full three-dimensional FEA simulations using a 23.5° half included tip angle and a 15 nm tip radius. Due to the symmetry involved, only a half space was modeled. Fig. 12 shows the inelastic equivalent strain contour maps at the maximum indentation depth (30 nm) for both the 11° tilted case and the normal indentation case. The load versus indentation depth curves obtained by FEA simulations were used to extract indentation modulus using the Oliver and Pharr method[1]. There was a 2.3% increase in the extracted indentation modulus by tilting the tip angle 11°, indicating that the slightly titled AFM tip is not going to be a major source of error for the conditions tested experimentally in this report.

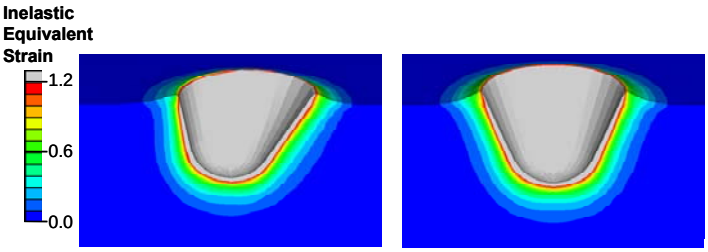

Figure 12. Full 3D FEA simulation results designed to assess the possible influence of an 11° tilted AFM tip with respect to the sample surface. The figure shows equivalent plastic strain contour plots at the maximum indentation depth (30 nm) for the 11° tilted case (left hand side) and the normal indentation case (right hand side). The inelastic strain distributions are similar in both cases. The extracted indentation modulus for the 11° tilted case had a 2.3% increase comparing to that for the normal indentation case. In all the simulations, the input modulus and yield stress (8.55 GPa and 395 MPa, respectively) were chosen as the average for the data taken from the map in Fig. 2b of the main manuscript, where the loading axis was perpendicular to the long bone axis. Here, the AFM probe tip was approximated as a cone tip with an included half angle of 23.5° and a 15 nm tip radius.

References

1. Oliver, W.C. & Pharr, G.M. An improved technique for determining hardness and elastic modulus using load and displacement sensing indentation experiments. *J. Mater. Res.* **7**, 1564-1583 (1992).
2. O'Brien, R.G. A general ANOVA method for robust test of additive models for variance. *J. Am. Stat. Assoc.* **74**, 877-880 (1979).
3. Tai, K., Qi, H.J. & Ortiz, C. Effect of mineral content on the nanoindentation properties and nanoscale deformation mechanisms of bovine tibial cortical bone. *J. Mater. Sci.- Mater. Med.* **16**, 947-959. (2005).
4. J.-Y., R. An ultrasonic method for measuring the elastic properties of human tibial cortical and cancellous bone. *Ultrasonics* **34**, 777-783 (1996).
5. Tai, K., Ulm, F.-J. & Ortiz, C. Nanogranular origins of the strength of bone. *Nano Lett.* **6**, 2520-2525 (2006).